Spray Characteristics of a Multi-hole Injector for Direct-Injection Gasoline Engines:
— **Source link** ↗

Nicholas Mitroglou, Jamshid M. Nouri, Manolis Gavaises, C. Arcoumanis

Institutions: City University London

Related papers:

- Spray Structure Generated by Multi-Hole Injectors for Gasoline Direct-Injection Engines

- Methods and Analysis of Fuel Injection, Mixture Preparation and Charge Stratification in Different Direct Injected SI Engines

- Internal Flow and Cavitation in a Multi-Hole Injector for Gasoline Direct-Injection Engines

- Automotive Spark-Ignited Direct-Injection Gasoline Engines

- Mechanisms of spray formation and combustion from a multi-hole injector with E85 and gasoline

Spray characteristics of a multi-hole injector for direct - injection gasoline engines

N. Mitroglou, J. M. Nouri, M. Gavaises and C. Arcoumanis
Centre for Energy and the Environment
School of Engineering and Mathematical Sciences, City University, London, UK

Abstract: *The sprays from a high-pressure multi-hole nozzle injected into a constant volume chamber have been visualised and quantified in terms of droplet velocity and diameter with a two-component phase Doppler amenometry (PDA) system at injection pressures up to 200bar and chamber pressures varying from atmospheric to 12bar. The flow characteristics within the injection system were quantified by means of an FIE 1-D model, providing the injection rate and the injection velocity in the presence of hole cavitation, by an in-house 3-D CFD model providing the detailed flow distribution for various combinations of nozzle hole configurations, and by a fuel atomisation model giving estimates of the droplet size very near to the nozzle exit. The overall spray angle relative to the axis of the injector was found to be almost independent of injection and chamber pressure, a significant advantage relative to swirl pressure atomisers. Temporal droplet velocities were found to increase sharply at the start of injection and then to remain unchanged during the main part of injection before decreasing rapidly towards the end of injection. The spatial droplet velocity profiles were jet-like at all axial locations, with the local velocity maximum found at the centre of the jet. Within the measured range, the effect of injection pressure on droplet size was rather small while the increase in chamber pressure from atmospheric to 12bar resulted in much smaller droplet velocities, by up to fourfold, and larger droplet sizes by up to 40%.*

Key words: *gasoline direct injection engines, high-pressure multi-hole injectors, phase Doppler anemometry, nozzle flow CFD simulation, atomisation modelling*

1. Introduction

The objective of introducing direct-injection gasoline engines into the market is to reduce fuel consumption through charge stratification under overall lean conditions, to increase volumetric efficiency and to reduce exhaust emissions. There are numerous feasible design configurations for spark-ignition gasoline direct injection engines, which are classified depending on the relative position of the injector to the spark plug and piston crown shape, the injection timing and the air motion and mixture preparation strategy. They are classified as wall-, air-, or spray-guided combustion systems, employing central or side fuel injection. In all concepts, good combustion is achieved by formation of a stable and ignitable mixture around the spark plug at the time of ignition. The major component of the fuel injection system that is responsible for preparing such a fuel/air mixture cloud is the high-pressure injector. Thus, knowledge of the spray characteristics, including spray structure, tip penetration and distribution of droplet velocities and diameters as a function of nozzle design, injection and chamber pressures, is essential.

Previously published investigations [1-8] have mainly focused on swirl pressure atomisers, known as first-generation injectors. In general, this type of injector can produce very finely atomised droplets with diameters (SMD) in the range 15-25µm over a moderate range of injection pressures (50-100bar). Their disadvantage is that the spray generated from these injectors is very sensitive to the operating and thermodynamic conditions. An unavoidable 'collapse', i.e. a reduction of spray angle and penetration at elevated chamber pressures (corresponding to the late-injection strategy of spray-guided systems) has been reported. A different type of injector, employing a multi-hole nozzle, has been recently introduced by fuel injection manufacturers, aiming to overcome this dependence of the spray characteristics on thermodynamic and operating conditions by introducing several holes in a configuration similar to diesel injector nozzles. Up to now there have been limited investigations on this type of injectors [9-12], who confirmed the improved stability of the spray at elevated chamber pressures relative to that of swirl injectors. Also, enhanced air entrainment has been observed due to the

separated spray jets, and the larger surface area, which can be independently directed at desired locations, achieving improved matching between the injector and the combustion chamber designs. There is a variety of multi-hole injector nozzle configurations that have been designed and manufactured, associated with the flexibility in hole positioning throughout the injector nozzle cap (e.g. 6 holes symmetrically distributed, 5 holes plus one in the centre, 12 holes, and all possible combinations as shown schematically in Fig.1).

In the present investigation a six-hole injector has been used to provide a quite symmetrical spray pattern. The aim is to quantify the effect of injection pressure up to 200bar and chamber pressure up to 12bar on the spray structure, using a pulsed light source and a CCD camera, and on the droplet velocities and sizes as measured with a phase-Doppler anemometer (PDA). The interpretation of the results is assisted by CFD simulations predicting the flow distribution within the injection system, in the nozzle tip itself and the near nozzle fuel atomisation process. The following sections describe the experimental arrangement, the measurement systems and the computer model, followed by presentation of the results and a summary of the main conclusions.

## 2. Experimental arrangement and instrumentation

A common rail system shown schematically in Fig.2, with the six-hole injector installed inside a constant-volume chamber, has been used in this investigation. A three-piston-type pump coupled to an electric motor is responsible for delivering high-pressure fuel (up to 200bar) to the common rail, which has been specifically built with one injector outlet. This common rail was connected to the injector via a pipe with specific diameter and length which was, in turn, fixed to the high-pressure chamber that is equipped with four quartz windows and connected to a pressurised bottle of nitrogen for maintaining the required back pressure inside the chamber (up to 25bar). A fuel pressure regulator attached to the common rail, a solenoid valve in the chamber's exhaust pipe and the injector were all controlled electronically.

Two prototype 6-hole injectors with a nominal overall spray cone angle of 90°, a hole diameter of ~140μm, forming an L/D (length/hole diameter) ratio of 2.14, and an operating pressure of up to 200bar were tested. The first one has a central hole with one of the side holes missing, while the second one has a symmetric hole arrangement. Tests have been carried out at two,

relatively high, injection pressures of 120 and 200bar and at four chamber pressures of 1, 4, 8 and 12bar. The duration of the injection triggering signal (i.e. the injection quantity) was kept constant at 1.5ms. Iso-octane has been selected as the working fluid, since it is safer to use and more convenient for optical studies than gasoline; it has a density, kinematic viscosity and surface tension of 692kg/m^3, 0.78cSt and 0.0188N/m, respectively.

Images of the spray were obtained with a time resolution of 50μs by a non-intensified, cooled CCD camera with a spatial resolution of 1280x1024 pixels, a sensitivity of 12bit and a minimum exposure time of 100ns. A strobe light of 20μs duration was used as the light source, which was synchronised to the camera.

A 2-D phase-Doppler anemometer shown schematically in Fig.3, has been used for the measurement of the axial and radial droplet velocities and diameters. According to the manufacturer, a droplet size range of 0.5μm to 100μm can be detected from the system and a typical accuracy of the measured size distributions is 4%, although it depends to a large extent on the optical configuration. The transmitting and receiving optics were installed on a 3-D traverse mechanism with a resolution of 12.5μm in the X, Y axes and 6.25μm in the Z axis, relative to the injector position. A wall-mounted Argon-Ion laser with a maximum power of around 1.5W was used and the output beam was aligned with the fibre optic unit.
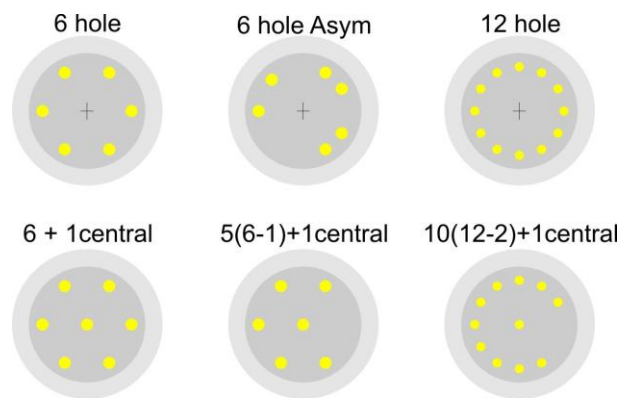
Fig. 1 *Schematic of possible multi-hole injector nozzle configurations (6-hole nozzles employ a L/D ratio of 2.14, while 12-hole nozzles appear to have twice the L/D ratio of the 6-hole nozzles).*
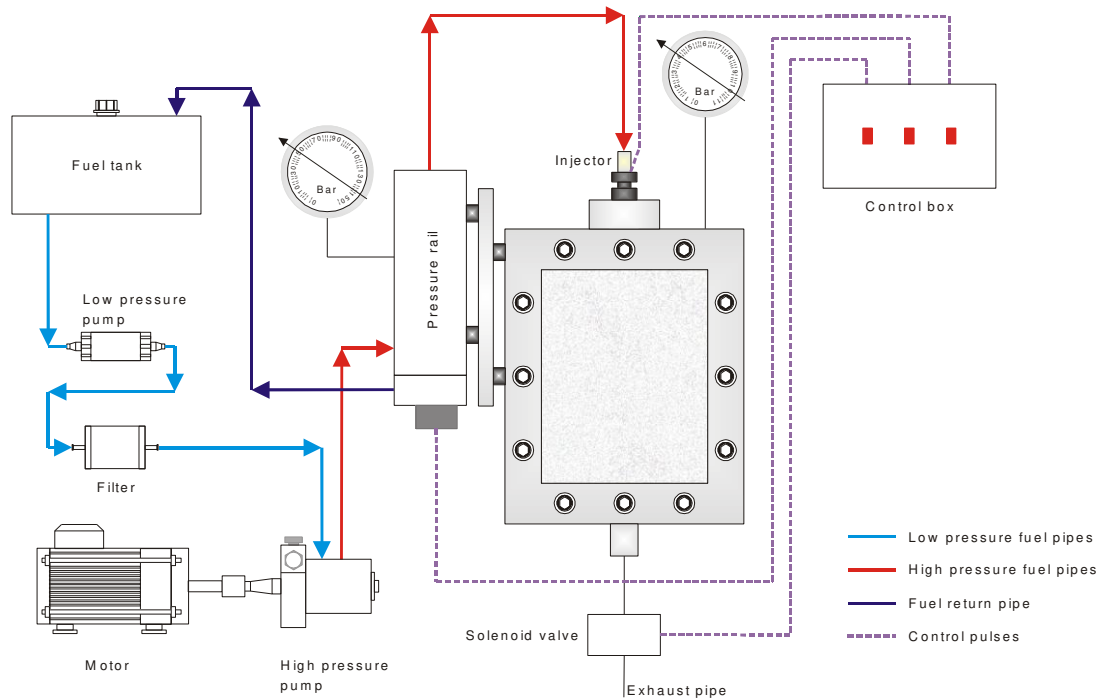
Fig. 2 *Schematic of the constant volume chamber test rig*

This unit was responsible for the splitting of the laser beam into two pairs of different wavelengths; each pair consisted of two equal intensity beams. The first pair was green light with a wavelength of 514.5nm, responsible for the axial velocity component, while the second pair was blue light with 488nm wavelength providing the radial velocity component.

A Bragg cell unit positioned inside this fibre optical unit provided a 40MHz frequency shift. The transfer of the four laser beams to the transmitting optics was through a fibre-optic cable. The collimating and focusing lenses formed an intersection volume with major and minor axes of approximately 2.863 and 0.092mm for the green, and 2.716 and 0.088mm for the blue component. Light scattered by the droplets was collected by a 310mm focal length lens positioned at 30° to the plane of the two incident green beams to ensure that refraction dominated the scattered light (Fig.3). The signal from the four photomultipliers was transmitted to the processor unit where all the data processing was carried out. The processor was connected to a desktop computer via an ethernet adaptor, where all the acquired data were saved for further analysis. Up to 1000 validated sample data were collected for each measurement location and a time window of 0.1ms over many injection cycles, to allow ensemble averages to be estimated. The measurements were synchronised with the needle lift by an external reset pulse, and restricted to the first 2.5ms after the start of the injection process, depending on the axial location and the pressure in the chamber.

Difficulties in measurements were encountered during the main injection period especially in the central part of the individual sprays jets and near the nozzle exit region under certain test conditions due to the attenuation of the incident laser beams and the scattered light. The problem was more pronounced in the case of injection against elevated chamber pressures, where the system was unable to detect adequate signals during the main part of injection up to an axial distance of 20 mm from the nozzle exit.
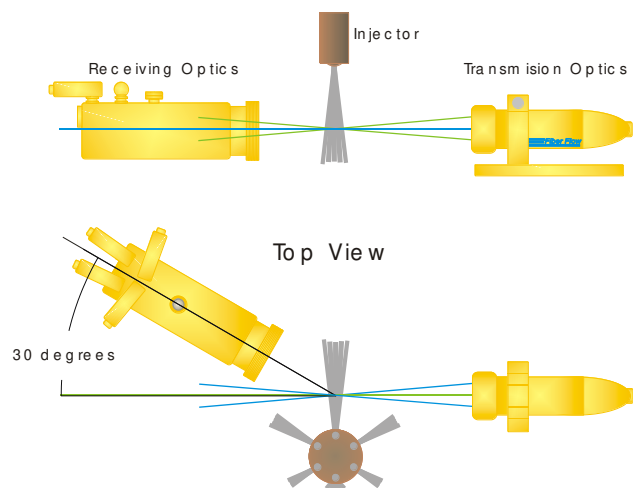
Fig. 3 *Optical configuration of the phase Doppler anemometer (PDA) system.*

3. Computer simulation model

In this section, the methodology employed in order to calculate the whole fuel injection process, that comprises the fuel injection system, the nozzle flow and the atomisation process of the injected sprays, is briefly described.

A variety of models have been applied to the simulation of the fuel injection process. Initially, a 1-D model has been used for the simulation of the pressure

waves developing inside the fuel injection system. The model is based on the solution of the mass and momentum flow conservation equations, expressed in 1-D, and which are solved numerically using the method of characteristics. It estimates the transient variation of the injection pressure inside the nozzle gallery and the flow rate through the discharge holes using as inputs the geometric characteristics of the rail, the connecting pipe and the nozzle itself as well as the nominal pressure value inside the common-rail. The needle lift, shown in Fig. 4, as well as the nozzle geometric details are additional inputs required by the model. The model used has been found to predict accurately the total fuel injection quantity as a function of injection pressure and injection duration, according to Fig. 5, for different needle lifts; a typical one is shown together with the triggering signal in Fig. 4. As can be seen, the volumetric capacity of the injector is almost a linear function of the triggering pulse width for injection durations greater than 1ms, but less so for shorter pulse durations. This is related to the fact that the needle opens fully at around 0.85 ms from triggering. It is also evident that the volumetric capacity of the injector at 200bar injection pressure is larger, as expected, than at 120bar.
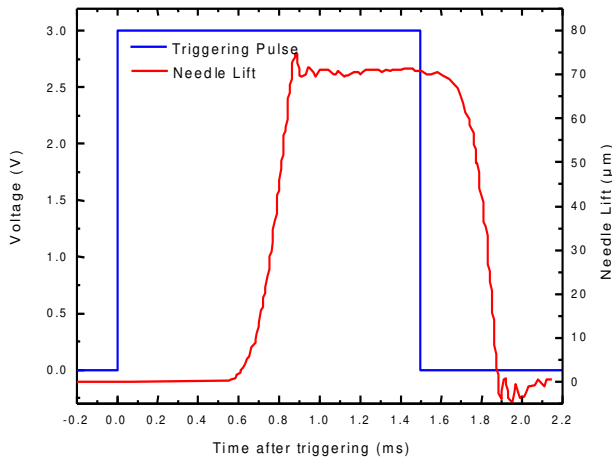

Fig. 4 *Triggering signal and typical needle lift diagram*
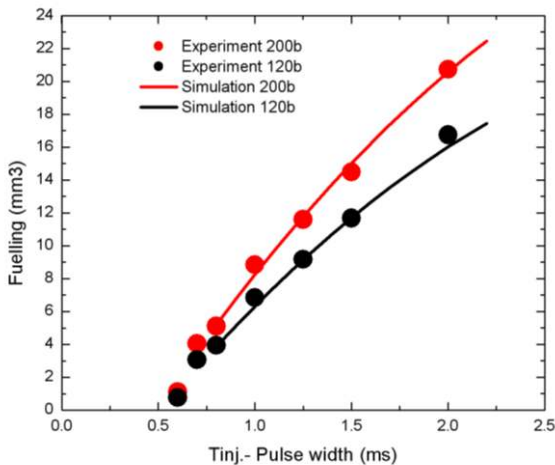

Fig. 5 *Volumetric capacity of the injector as a function of injection pulse duration under atmospheric conditions and for two injection pressures*

Past studies on hole-type nozzles have indicated that hole type nozzles such as that investigated here, cavitate above a threshold values for the injection pressure, for a given back pressure. Once cavitation initiates, then the discharge coefficient reduces asymptotically as function of the cavitation number [13], which is defined as $CN=(P_{UP}- P_{BACK})/(P_{BACK} - P_{VAPOR})$. An empirical formula allowing for such prediction is used here and the corresponding result is shown in Fig. 6b. This, in turn, can lead to the prediction of the hole effective area, which is the percentage of the cross sectional hole exit area occupied by liquid, with the remaining part assumed to consist of cavitating bubbles. In the case of cavitating nozzle flow conditions, the effective area decreases with increasing cavitation number (or injection pressure), as shown in Fig. 6a. The value of the hole effective area is a measure of the increase of the injection velocity as a result of the formation of cavitation relative to that under non-cavitating conditions. More details about this simple hole cavitation model as well as the 1-D fuel injection system model can be found in [14].
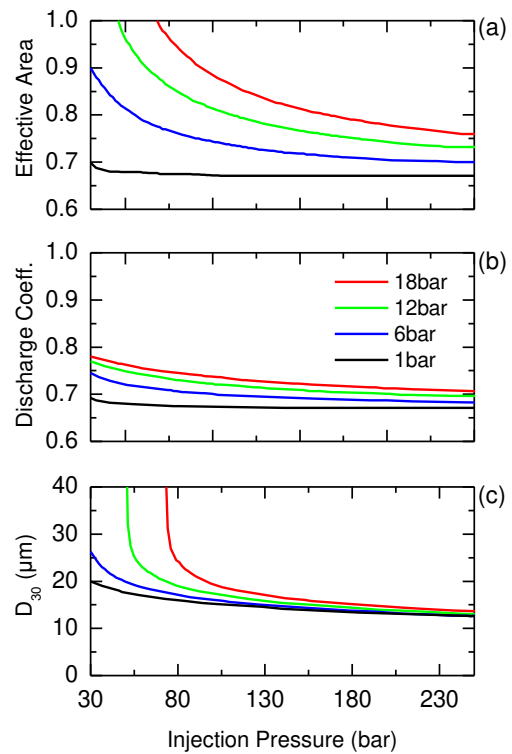

Fig. 6 *Predicted nozzle hole effective area (a), hole discharge coefficient (b) and droplet volume mean diameter (c) as a function of injection pressure for different chamber pressure values.*

For the simulation of the detailed flow distribution inside the sac volume and the injection holes, a multi-dimensional turbulent CFD flow solver, named GFS, has been employed. The time-averaged form of the incompressible Navier-Stokes equations describing the continuity, momentum and conservation equations for scalar variables were numerically solved on an unstructured non-orthogonal and curvilinear numerical

grid using collocated Cartesian velocity components. Turbulence was simulated by the two equation k-ε model. The discretisation method was based on the finite volume approach and the pressure correction method used was based on the PISO algorithm. A more detailed description can be found in [15]. A typical numerical grid used for the simulation of the nozzle flow is shown in Fig. 7.
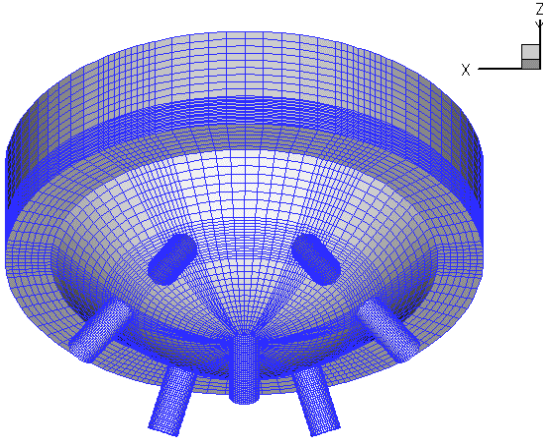
Fig. 7 *Typical numerical grid used for the simulation of the flow in the sac volume and the injection holes.*
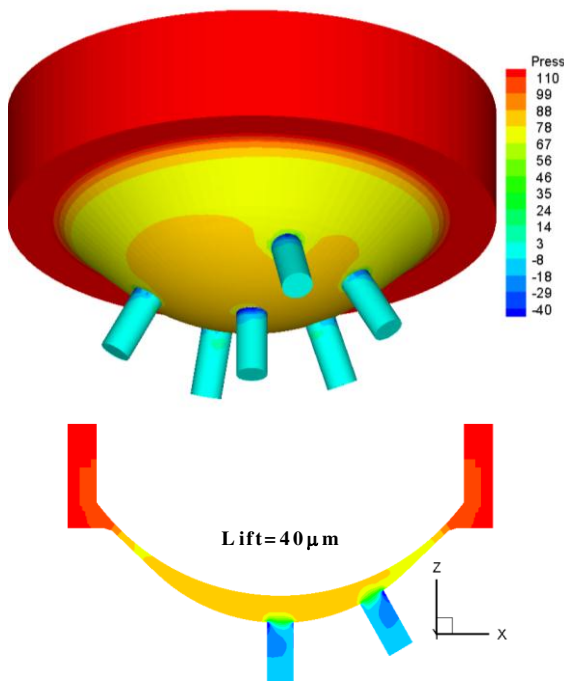
Fig. 8 *Predicted pressure distribution inside the injection nozzle as a function of the needle lift, showing the pressure drop taking place at the needle seat area. The low pressure (cavitation) region formed at the hole entrance can be seen clearly even at very low needle lifts.*

Following its injection, the fuel disintegrates into a large number of liquid droplets, which form the spray plume. The detailed process is difficult or even impossible to be described using direct numerical simulation, due to the large number of parameters involved, associated with the presence of the cavitating

bubbles exiting from the injection hole together with the liquid. To address the problem in an engineering manner, a phenomenological cavitation-induced atomisation model previously used for diesel spray simulations has been employed. Nevertheless, modifications were required to the original model in order to accurately predict the measured droplet size distribution near the nozzle. Overall, the model predicts a reduction of the droplet volume mean diameter D_{30} with increasing injection pressure, as shown in Fig. 6c. The predicted values reach asymptotically a minimum value of around 20μm for injection pressures in excess of 200bar and atmospheric chamber pressure.

4. Results and discussion

### 4.1 Internal nozzle flow and near-nozzle spray characteristics

The first set of results to be presented refers to the internal nozzle flow and its effect on the near-nozzle spray characteristics. Since in this area reliable measurements are very difficult to be obtained, the computer model has been used to provide an indication of the detailed two-phase flow processes.

The internal nozzle flow is mainly determined by the pressure drop at the needle seat area and the entrance to the injection holes. For the particular injector design investigated here, the needle seat pressure drop can be substantial relative to the rail pressure, as shown in Fig. 8 for a needle lift of 40μm. This is reflected in the spray velocity and the resulting droplet size during the transient phase of the needle opening and closing. During that period, droplet velocities are much smaller than in the main injection phase and droplet diameters significantly larger. Also, even at full lift, the actual injection pressure is about 90% of the rail pressure. At the entrance to the injection holes, the local pressure falls well below the vapour pressure of the liquid, indicating that cavitation is expected to take place in this area. For the side holes, the fluid volume under negative pressure is located at the 'top' of each injection hole. As can be seen in Fig. 9, according to the streamlines inside the sac volume that are coloured relative to the total velocity of the liquid, most of the fuel entering those holes is coming directly from above. However, for the central hole, cavitation is present all around the periphery of the nozzle inlet. Again from Fig. 9, it can be deduced that for the central hole the liquid is entering from the side area where one hole is missing, but also from the space between adjacent side holes. The liquid coming from that space splits into three parts. The central part is heading towards the central hole, but at the point where it mixes with the opposite side flow, just upstream of the hole entrance, two side jets are formed and create various recirculation zones. Part of that

liquid is forming stagnation points within the sac volume, believed to be candidate areas for internal cocking formation, and part enters into the side holes from the 'bottom'. This turbulent and unsteady flow structure leads to the central hole injecting more fuel relative to the rest, while the flow itself becomes more unsteady as higher turbulent kinetic energy values are predicted. At the same time, as the CCD spray images have revealed, the spray penetrates faster and with significant shot-to-shot variations. An indicative spray image from that injector is shown in Fig. 10. Since this injector design (5+1 central) has been found to give undesirable spray patterns, the remaining of the results to be presented later on refer to the symmetric six-hole nozzle configuration.
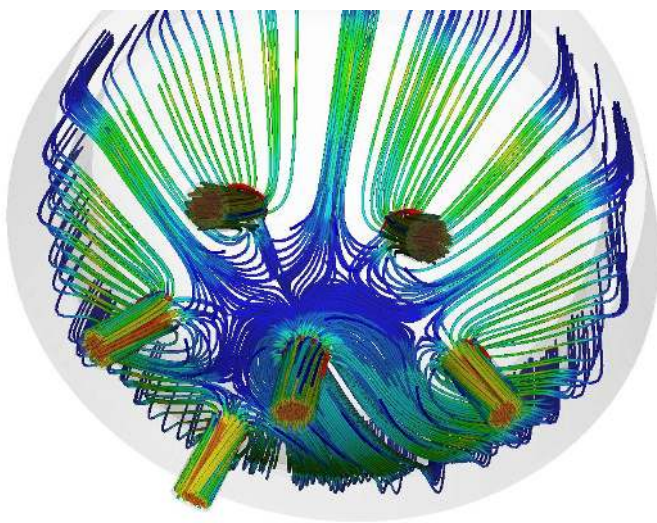

Fig. 9 *Streamlines of the internal nozzle flow for the injector with the central hole. The flow is unevenly distributed between the various holes, leading to an unstable pattern in the central hole.*
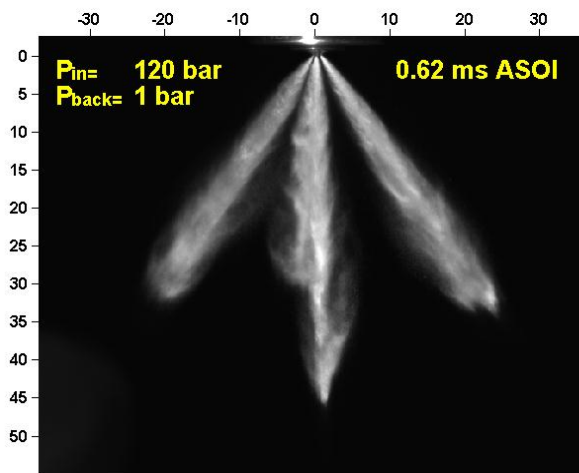
Fig. 10 *CCD Image from a 5+1 central hole nozzle configuration showing the over-penetration of the central hole relative to the side ones*

Fig. 11 shows the predicted injection velocity during the 1.5ms injection period, for two injection pressures of 120 and 200bar. Predictions based on both the geometric hole-area and the effective hole area are presented. Clearly their differences are of the order of 25-30%. LDV measurements of the droplet velocities measured as close as 2mm from the nozzle exit confirm that the injection velocity, and thus the spray momentum, is controlled by cavitation, since the measurements fall very close to the predictions obtained with the effective hole area flow model. Thus, cavitation in multi-hole gasoline injectors is an important flow characteristic, similar to diesel injectors. Its effect on the droplet size just at the nozzle exit can be also quantified using the cavitation-induced atomisation model. Figure 12 shows the droplet sizes just at the nozzle exit as predicted for the two injection pressures of 120 and 200bar, and for atmospheric chamber conditions. As already mentioned, during the opening and closing phases of the needle, the predicted droplet diameters are larger when compared to the main injection. On the same graph, PDA measurements obtained on a plane located 10mm from the nozzle exit and averaged over all measurement points, show that predictions are quite reasonable. In turn, this indicates that cavitation is mainly responsible for the disintegration of the liquid jet emerging from the nozzle hole.

Having determined the internal nozzle flow structure and its effect on the near-nozzle spray characteristics, we can now proceed to the presentation of the measurements obtained for characterising the spray further downstream.
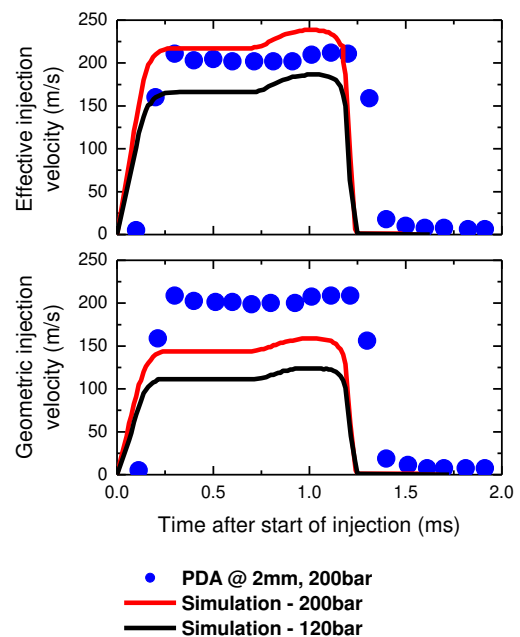
Fig. 11 *Predicted results for the injection velocity based on the geometric and the effective hole area for injection pressures of 120 and 200bar and chamber pressures of 1bar. They are validated against experimental (PDA) data of the injection velocity at 200bar, obtained 2mm downstream of the injection hole exit.*
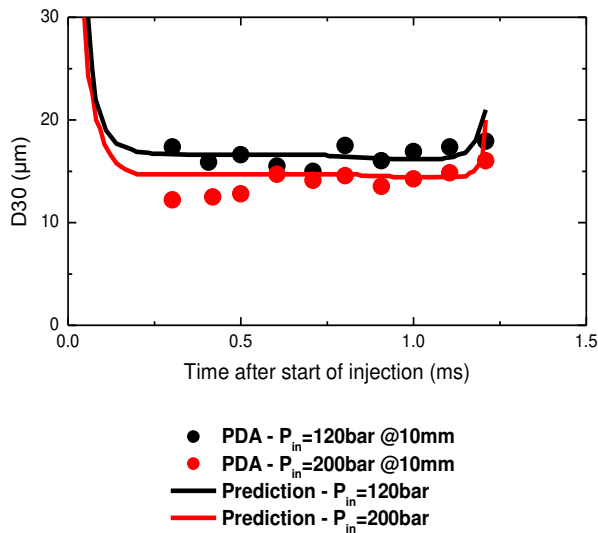
Fig. 12 *Predicted D30 of the formed droplets for two different injection pressures of 120 and 200bar. They are validated against PDA measurements of the droplet size obtained under atmospheric conditions 10mm downstream of the injection hole.*

4.2 Spray characteristics

Images of the spray development as a function of time after the start of injection were obtained at two injection pressures, 120 and 200bar, and four chamber pressures of 1, 4, 8 and 12bar. The injection duration was 1.5ms in all test cases investigated. A typical sequence of the obtained images is shown in Figs.15 and 16. Quantitative spray characteristics, such as droplet velocities and diameters, were obtained at two injection pressures (120 and 200bar) and two chamber pressures (1 and 12bar); they are presented in Figs.18-23 for axial distances (z) of 10 and 30 mm from the nozzle exit.

4.2.1 Spray imaging

Spray images have been obtained using a CCD camera, which was synchronised with the injection pulse. The images revealed that the injector needle opening delay time relative to the triggering signal was about 0.6ms, while the end of injection was at about 1.8ms. This resulted in an actual injection duration of 1.2ms for a triggering signal of 1.5ms duration. The needle opening and closing delay times proved to be quite independent of the injection pressure and chamber pressure. These effects can be clearly seen in the needle lift curve (Fig.4).

The spray cone angle and tip penetration data were obtained by post-processing of the images, which quantified their dependency on injection conditions. A bottom view of the injector nozzle shows that the 6 holes are evenly distributed on the periphery of a circle, whose centre is the axis of symmetry of the injector. The plane where the overall spray angle was calculated is shown in Fig.13; the angle is measured between the axes of the two outer jet sprays. The results showed a constant overall

spray angle, independent of injection and chamber pressure, with a mean value estimated to be 80°±1.5° under all conditions tested; this remained unchanged at all axial distances from the nozzle exit.
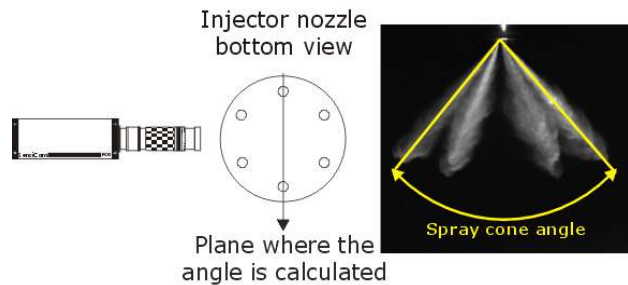

Fig. 13 *Overall spray angle definition*

Data extracted from the images also revealed useful information about the spray tip penetration. The multi-hole spray consists of individual jets and the penetration of the spray is defined as the axial distance between the nozzle exit and the tip of each jet. In Fig.14 a comparison of the spray penetration curves for the two injection and chamber pressures is presented. The values plotted represent the mean over 20 single-shot images acquired consecutively. All jets in every single shot image proved to have nearly identical penetration. As expected, spray penetration increases with injection pressure and decreases with increasing chamber pressure.
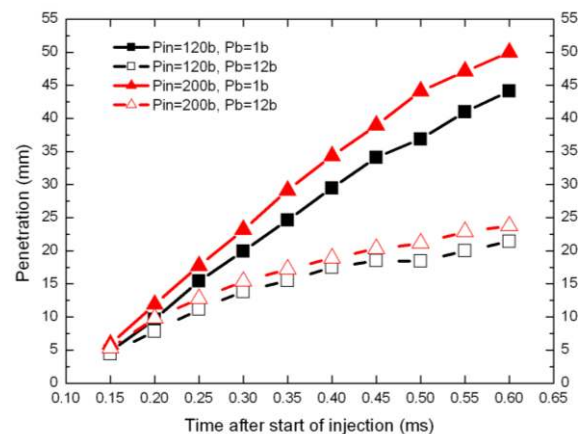
Fig. 14 *Spray penetration for two different injection and back pressures as estimated by averaging over 20 CCD spray images*

The effect of back-pressure is evident not only in the spray penetration curves but also in the individual spray images shown in Fig. 15. For injection against atmospheric chamber pressure, the individual sprays are thin and long relative to those corresponding to 12bar which are more dense, with a bushy shaped tip; nevertheless, the overall spray cone angle remains the same at both chamber pressures, providing strong justification for the use of these injectors in direct-injection gasoline engines.

(a)   (b)
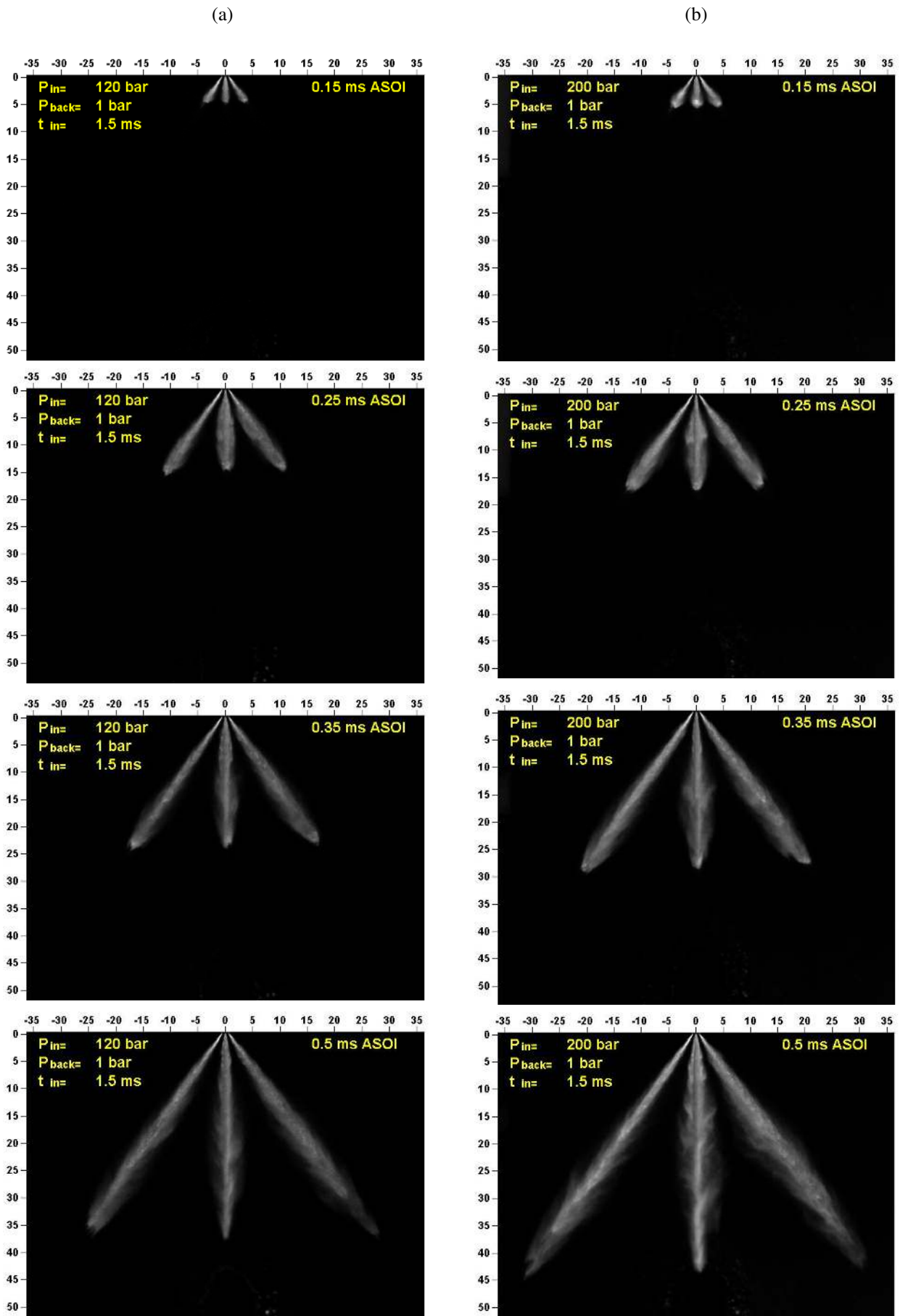
Fig. 15 *Time-dependent comparison of spray injected at two injection pressures: a 120bar and b 200bar for atmospheric chamber pressure*
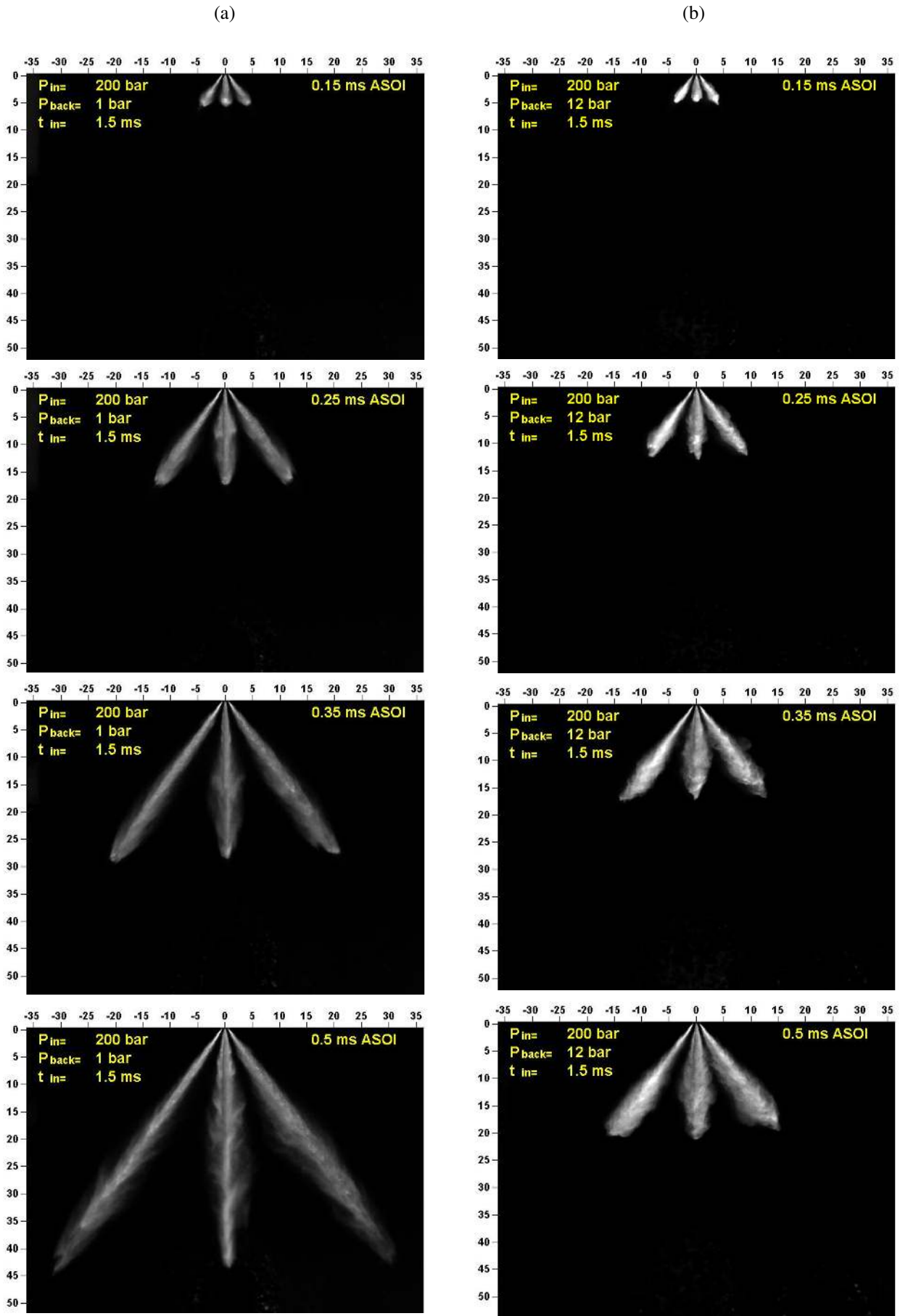
(a)

(b)

Fig. 16 *Time-dependent comparison of spray injected at two chamber pressures: a 1bar and b 12bar for a 200bar injection pressure*

4.2.2 Droplet velocity and size distribution

The temporal and spatial distributions of droplet velocity and diameter were obtained using a 2-D PDA system at two different axial distances from the 6-hole fully symmetric injector, z=10 and 30 mm, as shown in Fig. 17. Due to the symmetric arrangement of the holes in the sac-volume, a fully symmetric in-nozzle flow is expected. Measurements have thus been focused on one spray jet, assuming close similarity amongst all six jet plumes. Measurements have been obtained for chamber pressures of 1 and 12bar, injection pressures of 120 and 200bar and an injection duration of 1.5ms. Ensemble averaged values of the droplet mean and root mean square. (RMS) velocities and the arithmetic mean (AMD) and Sauter mean (SMD) droplet diameters were estimated over 0.1 ms time intervals.

The temporal variation of droplet velocity and diameter in the centre of one of the sprays at 10 mm from the injector is shown in Fig.18 and quantifies the effect of injection pressure. The mean axial and radial droplet velocities, plotted in Fig.18a, show similar trends with a sharp increase in velocities in the leading edge of the spray, nearly constant values during the main part of injection and a sharp drop in the trailing edge of the spray. The droplet velocity fluctuations of both components follow the mean velocity variation with a uniform distribution during the main part of the spray. The effect of increasing injection pressure is to generate larger mean and RMS droplet velocities, as expected, so that during the main part of the spray (from 0.5 to 1.5ms) the average axial mean and RMS velocities are 120 and 20 m/s at 200bar injection pressure and 95 and 15m/s at 120bar, respectively, the corresponding values for the radial velocity component are 100 and 18m/s at 200bar and 77 and 15m/s at 120bar, respectively. The spray angle relative to the axis of the injector could be calculated from the two velocity components; during the main part of the spray the jet angles are 78.6° and 78° at injection pressures of 200 and 120bars, respectively, which are very similar confirming the stability of the sprays injected from multi-hole nozzles. Also the angles are in good agreement with the values (80°) estimated from the spray images, providing further confidence in the PDA velocity measurements.
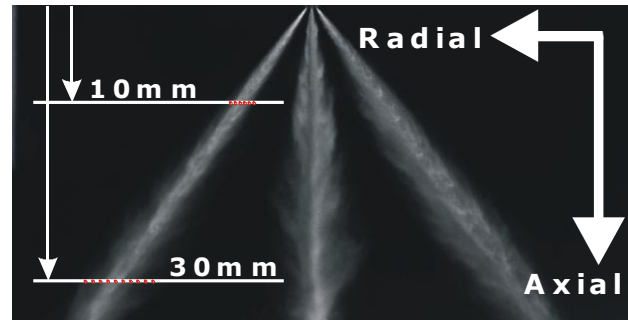

Fig. 17   *PDA measurement grid*

The size distribution, shown in Fig.18b, shows a gradual increase in droplet size in the leading edge of the spray, almost constant values during the main part of the spray and a gradual decrease in the trailing edge of the spray. The AMD and SMD values at the higher injection pressure are slightly lower with average AMD values of around 15 and 13µm at injection pressures of 120 and 200bar, respectively, representing a difference of around 13%; the corresponding SMD values are 27 and 22µm, giving a difference of around 18%.

Fig. 18   *Temporal variation of* (a) *droplet velocity and* (b) *droplet diameter, at injection pressures of 120 and 200bar, chamber pressure of 1bar at 10mm axial location from nozzle exit.*
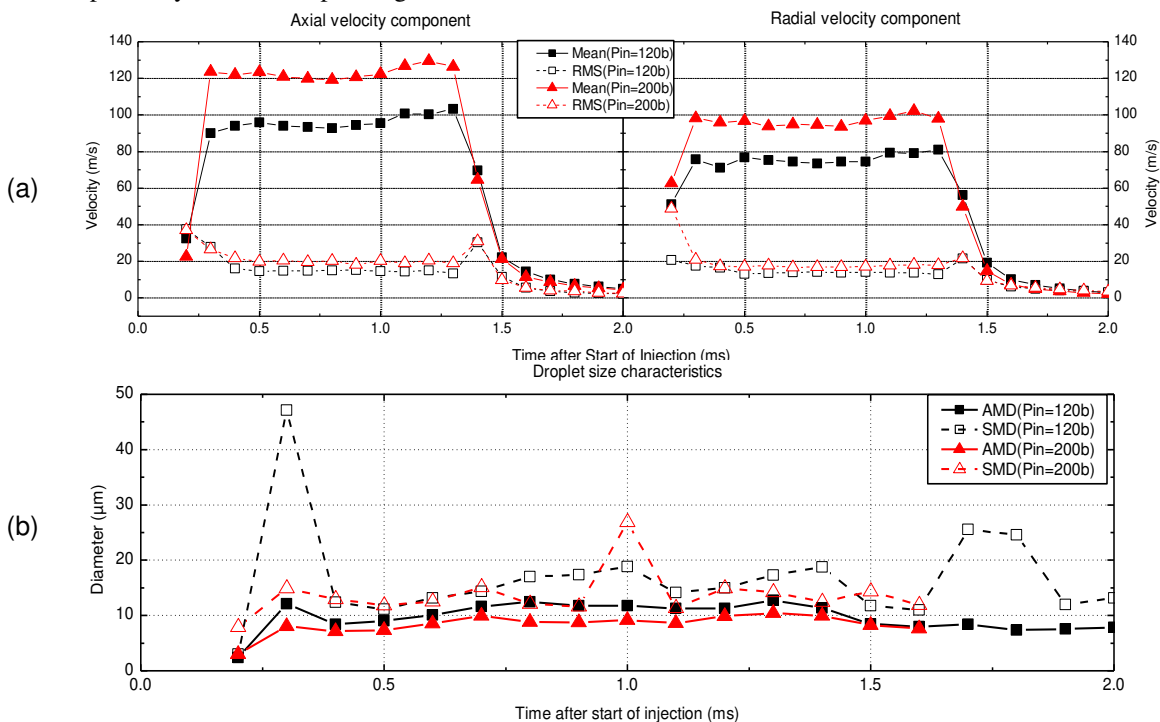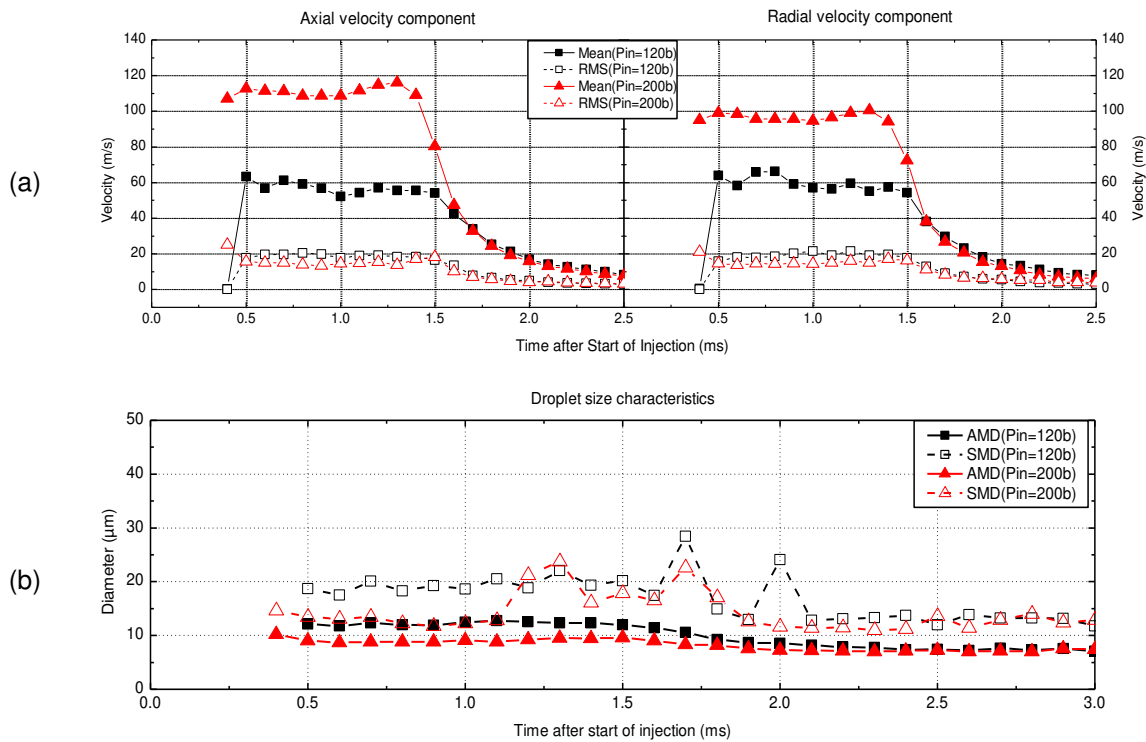
Fig. 19 *Temporal variation of* (a) *droplet velocity and* (b) *droplet diameter, at injection pressures of 120 and 200bar, chamber pressure of 1bar at 30mm axial location from nozzle exit.*

Figure 19 presents similar results to those of Fig.18 but further away from the injector at an axial location of 30 mm. Droplet mean and RMS velocity measurements are plotted in Fig.19a for the two velocity components demonstrating an overall reduction in mean velocities, but similar RMS values relative to the measurements obtained at 10mm. The droplet sizes shown in Fig.19, also present similar trends to those at 10 mm from the injector but with an overall reduction in AMD and SMD values. In particular, during the main part of the spray, the average AMD values are 12 and 9μm at injection pressures of 120 and 200bar, respectively, while the corresponding SMD values are 19 and 14μm, respectively. These values suggest that the overall droplet diameters at 200bar injection pressure are lower than those at 120bar by about 25% for both AMD and SMD, demonstrating the obvious advantages on fuel atomisation of high pressure injectors.

Figure 20 presents the temporal variation of droplet velocities and diameters at the spray centre at the same distance of z=30 mm and 200 bar injection pressure but for two chamber pressures of 1 and 12bar. The effect of chamber pressure on droplet velocities, shown in Fig.20, is clearly evident leading to substantially reduced mean velocities for both components at 12bar chamber pressure during the main part of the spray by more than threefold; the reduction in the RMS velocities is up to 50% during the same period. However, the droplet mean and RMS velocity values tend to be similar at both chamber pressures in the tail of the spray. It is also evident from the results that the droplet arrival time at z=30mm has

been delayed by 0.5ms at the 12bar chamber pressure case, which is in agreement with the reduction in the spray penetration length estimated from the CCD images. The spray angle to the axis, as calculated from the mean axial and radial velocities, was found to be 80 ± 2° during the main phase of the spray for both chamber pressures, demonstrating the independence of the overall jet angle on chamber pressure, in agreement with the spray visualisation results. It is useful to stress the importance of spray angle stability in spray-guided systems where successful ignition depends on the precise delivery of the spray edge recirculation onto the spark plug gap at the time of ignition.

The effect of chamber pressure on the droplet sizes is demonstrated in the results shown in Fig.20, which reveal a considerable increase in droplet diameter at elevated chamber pressures. For example, during the main part of the spray the average values of AMD and SMD at atmospheric chamber pressure are 10 and 15μm, respectively, while at 12bar those values increase to 18 and 25μm, respectively.

The spatial distribution of droplet velocities and diameters across the jet at z=10 mm from the injector and at 1ms after the start of injection is shown in Fig.21 for injection pressures of 120 and 200bar. The mean velocity profiles across the spray diameter at both injection pressures exhibited a jet like distribution with the peak corresponding to a radial position of 8.5-9.0mm from the injector axis as shown in Fig.21a; the RMS velocity distribution, on the other hand, was more uniform.
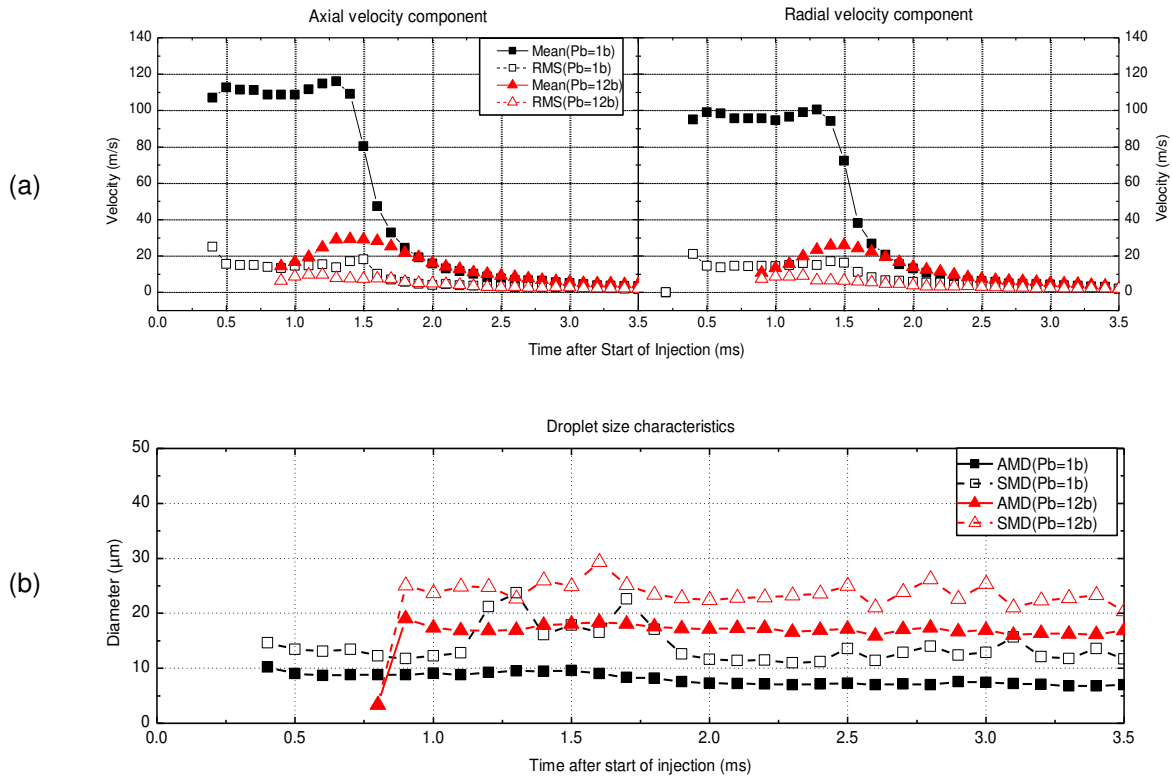
Fig. 20 *Temporal variation of* (a) *droplet velocity and* (b) *droplet diameter, at injection pressure of 200bar, chamber pressures of 1bar and 12bar and axial location 30mm from nozzle exit.*
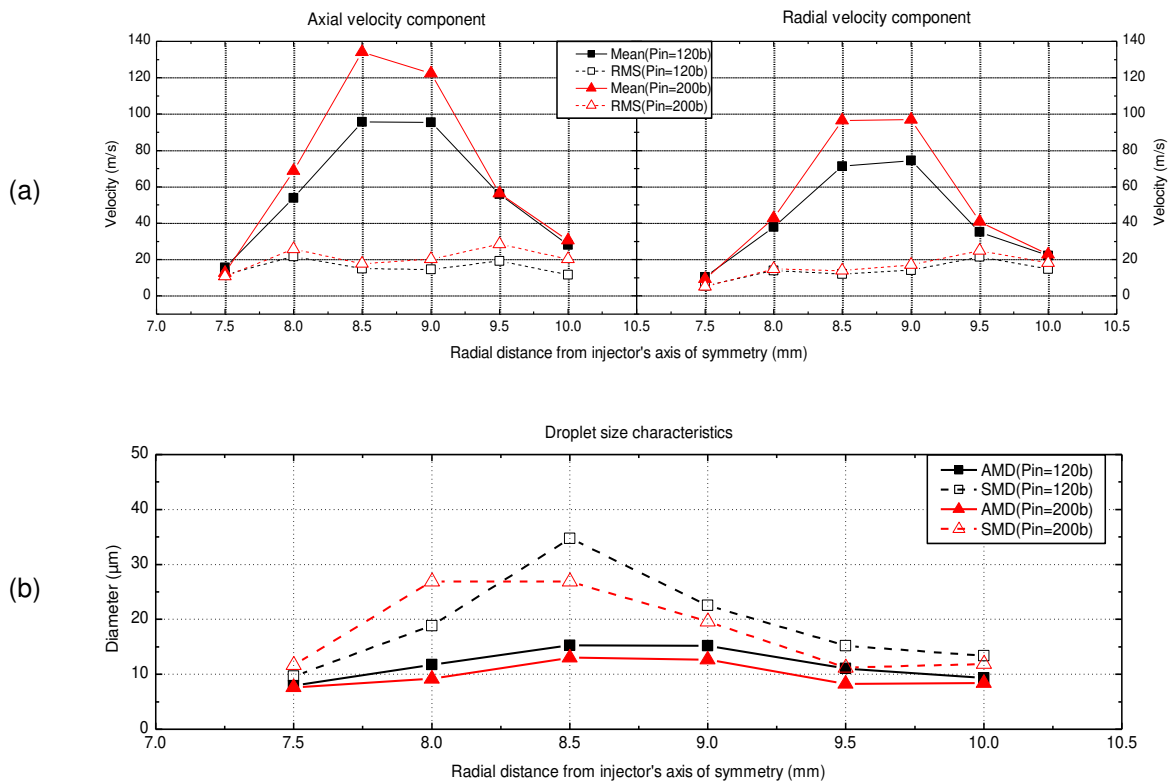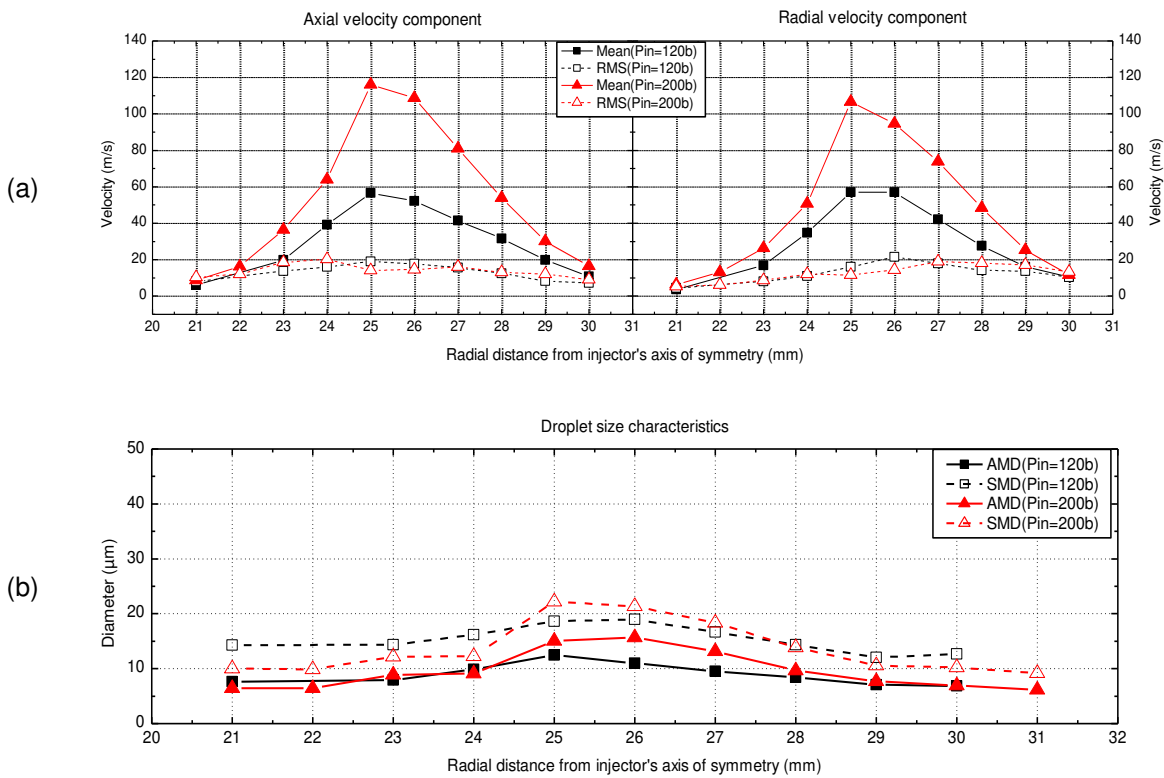

Fig. 21 *Spatial variation of* (a) *droplet velocity and* (b) *droplet diameter, at injection pressures of 120 and 200bar, chamber pressure of 1bar and axial location 10mm from nozzle exit.*

The droplet diameter radial distribution shown in Fig.21b for the same conditions, follows the trend of the mean velocity profile with a gradual increase to a maximum value at around the spray axis and a gradual decrease towards the edges. As for the effect of injection pressure on the droplet velocity and diameter, it is similar to that described previously, in that the higher injection pressure gives rise to higher droplet velocities and smaller droplet diameters.

Further downstream at z=30mm the droplet diameter distribution shown in Fig. 22 follows the same trend as at 10mm. However, both the AMD and SMD values are reduced at 30mm compared to those at 10mm over the whole cross-section. This suggests that droplets are undergoing a secondary break up as the spray develops downstream.

Finally, Fig. 23 quantifies the effect of chamber pressure on the droplet velocities and diameters over the whole cross-section of the spray at z=30 mm from the nozzle exit and 200bar injection pressure. The effect of the increased chamber pressure on droplet velocities, shown in Fig.23a, is clearly evident. The mean velocity of both velocity components is reduced substantially at 12bar chamber pressure over the whole cross-section by up to four times due to the higher drag, and that the droplet velocity fluctuations are also reduced by a factor of two during the same period. Fig. 23b presents the effect of chamber pressure on droplet sizes and it clearly shows a considerable increase in the droplet diameter when the chamber pressure increases from 1 to 12bar. The average values of AMD and SMD around the centre of the spray at atmospheric chamber pressure are 15 and 20μm, respectively, while the corresponding values at 12bar chamber pressure are 19 and 28μm, which corresponds to a 25% increase for the AMD and a 40% increase for the SMD, respectively.

Fig. 22 *Spatial variation of* (a) *droplet velocity and* (b) *droplet diameter at injection pressures of 120 and 200bar, chamber pressure of 1bar and axial location 30mm from nozzle exit.*
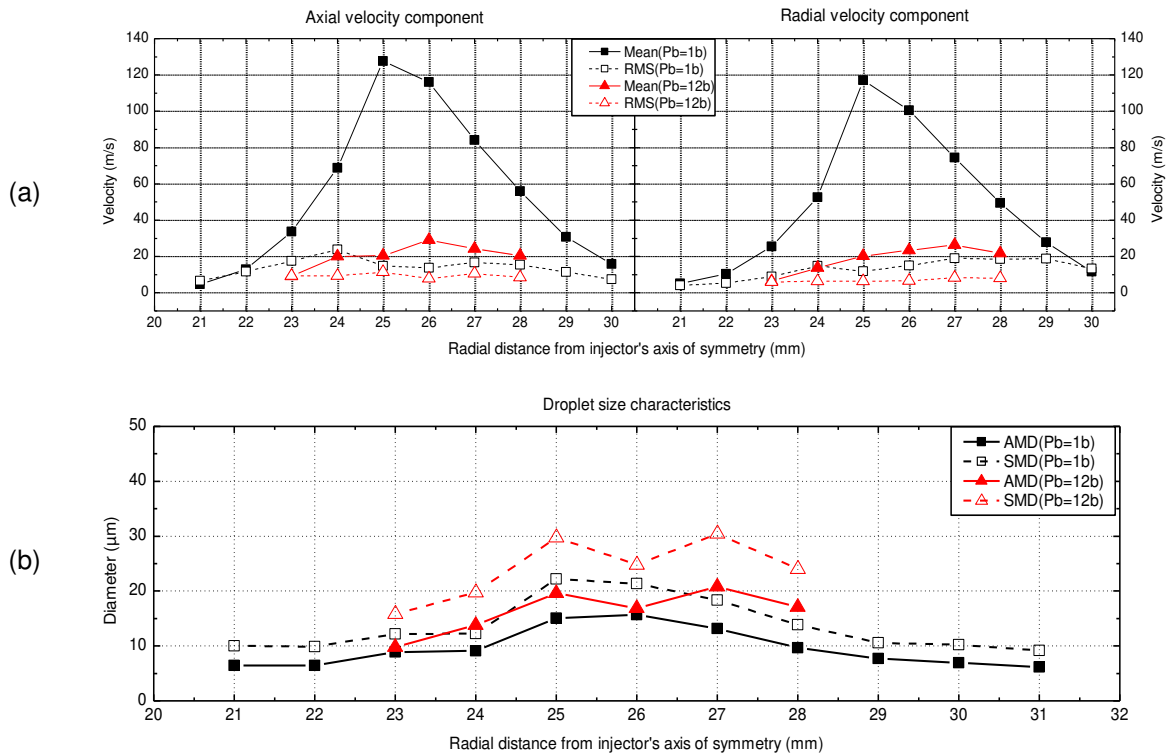
Fig. 23 *Spatial variation of* (a) *droplet velocity and* (b) *droplet diameter at injection pressure of 200bar, chamber pressures of 1bar and 12bar and axial location 30mm from nozzle exit.*

4. Conclusions

The sprays generated from multi-hole injectors, introduced recently in spray-guided direct injection gasoline engines, have been characterised in terms of droplet velocities/diameters at injection pressures of 120 and 200bar and chamber pressures varying from atmospheric to 12bar. Additional spray visualisation has confirmed that the spray angle remains constant and is almost independent of injection and chamber pressure, a significant advantage relative to pressure-swirl atomisers used in the first-generation, wall-guided gasoline engines.

The internal nozzle flow and the near nozzle spray characteristics have been estimated by employing a combination of computer models. Those comprised a 1-D model simulating the flow inside the injection system, a 3-D Navier-Stokes equations flow solver simulating the sac-volume and injection holes and a phenomenological nozzle hole cavitation. In addition, a cavitation-induced atomisation model was used to provide estimates of the liquid velocity increase due to hole cavitation and the corresponding effect on the size of the droplets formed during the atomisation process of the injected fuel. The results have shown that cavitation is the main flow factor that determines injection velocity and initial droplet size. At the same time, internal flow simulations have shown that multi-hole injectors with a central hole have an uneven flow distribution which results to an over

penetrating and unstable spray pattern, as also confirmed by CCD spray images.

The droplet temporal velocity profiles revealed that the droplet velocities increased sharply at the start of injection to a maximum value and then remained unchanged during the main part of injection before decreasing rapidly towards the end of injection. The spatial velocity profiles were jet-like at all axial locations with the local velocity maximum found on the spray axis. The droplet SMD in the main spray at 10mm from nozzle exit were of the order of 19 and 14μm at injection pressures of 120 and 200bar, respectively, for injection against atmospheric chamber pressure. Within the measured range the effect of injection pressure on droplet size was small while the increase in chamber pressure to 12bar resulted in a large decrease in droplet velocities by up to fourfold and an increase of droplet sizes by up to 40%.

Overall, the obtained results have confirmed the advantages of new generation high-pressure multi-hole injectors for gasoline direct-injection engines, compared to swirl pressure atomisers, in terms of spray structure stability under varying chamber thermodynamic and injector operating conditions. Nevertheless, their ability to generate the desired air/fuel mixture at the spark plug at the time of ignition with minimum nozzle cocking remains an issue. At present, a lot of effort and resources are devoted to identifying the best injection system for second-generation gasoline engines employing the spray-

guided concept under stratified operation. It seems that the degree of success of the spray-guided concept will determine whether direct-injection gasoline engines will make an impact onto the passenger car market at a time of increasing competition from advanced direct-injection diesel engines. It is likely that spray-guided gasoline engines operating with stoichiometric mixtures under naturally aspirated or turbocharged conditions will be the first to enter production prior to the most fuel efficient, albeit more difficult, stratified direct-injection, gasoline engines. Stoichiometric engines offer significant advantages in terms of volumetric efficiency and reduction of charge temperature (allowing higher compression ratios to be used) while at the same time maintaining the benefits of three-way catalysts in reducing all three major gaseous pollutants.

Acknowledgement

References

1 **Shrimpton, J. S., Yule, A. J., Akhtar, P., Wigley, G.** and **Wagner, T.** Measurement in diesel sprays for three fuels with and without cross flow of high-pressure gas. Proc. ILASS, 1997.

2 **Shelby, M. H., VanDerWege, B. A.** and **Hochgreb, S.** Early spray development in gasoline direct-injection spark-ignition engines. SAE 980160, 1998.

3 **Wigley, G., Hargrave, G. K.** and **Heath, J.** A high power, high resolution LDA/PDA system applied to dense gasoline direct-injection spray. 9th Int. Symp. Appl. Laser Tech. to Fluid Mechanics, 1998.

4 **Abo-Serie, E., Arcoumanis, C.,** and **Gavaises, M.** Structure of sprays generated by pressure swirl atomisers for direct-injection gasoline engines. ILASS Symposium, 1999.

5 **Ipp, W., Wagner, H. K., Wensing, M., Leipertz, A., Arndt, S.** and **Jain, A. K.** Spray formation of high-pressure swirl gasoline injectors investigated by two-dimensional Mie and LIEF techniques. SAE 1999-01-0498, 1999.

6 **Nouri, J. M.,** and **Whitelaw, J. H.** Spray characteristics of a GDI injector with short injection duration. Exp. Fluids, 2001.

7 **Nouri, J. M., Brehm, C.** and **Whitelaw, J. H.** The spray from a gasoline direct injector. ILASS Symposium, 1999.

8 **Gavaises, M.** and **Arcoumanis, C.** Modelling of sprays from high pressure-swirl atomisers." International Journal of Engine Research 2, 2001.

9 **Ortmann, R., Arndt, S., Raimann, J., Grzeszik, R.** and **Wurfel, G.** Methods and analysis of fuel injection, mixture preparation and charge stratification in different direct-injected SI engines. SAE 2001-01-0970, 2001.

10 **Arndt, S., Gartung, K.** and **Bruggemann, D.** Influence of ambient temperature on the evaporation rate of hexadecane droplets Proc. ILASS-Europe 2001.

11 **Lippert, A. M., El Tahry, S. H., Huebler, M. S., Parrish, S. E., Inoue, H., Noyori, T., Nakama, K.** and **Abe, T.** Development and optimisation of a small-displacement spark-ignition direct-injection engine – Stratified operation. SAE 2004-01-0033, 2004.

12 **Pontoppidan, M., Gaviani, G., Bella, G.** and **De Maio, A.** Optimisation by CFD simulation of spray formation parameters to adapt direct-injection high-pressure fuel injectors to high-speed SI engines. SAE 2004-01-0539, 2004.

13 **Soteriou, C., Andrews, R.,** and **Smith, M.,** Direct injection diesel sprays and the effect of cavitation and hydraulic flip on atomization, SAE 950080, 1995.

14 **Arcoumanis, C., Gavaises, M.** and **French, B.** Effect of fuel injection processes on the structure of diesel sprays. SAE 970799, 1997.

15 **Gavaises, M., Tonini, S., Arcoumanis, C., Kometani, S.** and **Theodorakakos, A.** Multi-component fuel vaporisation and its effect on spray development and air-fuel mixing in gasoline direct-injection engines, 5th International Conference ICE2003 Internal Combustion Engines: Experiments and Modelling, 2003.